Sensors & Actuators: B. Chemical 327 (2021) 128903

Contents lists available at ScienceDirect

Sensors and Actuators: B. Chemical

journal homepage: www.elsevier.com/locate/snb

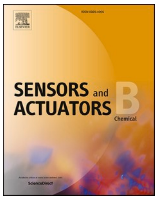

Enhanced semiconductor charge-transfer resonance: Unprecedented oxygen bidirectional strategy

Yingnan Quan[a,b,c], Jiacheng Yao[a,b,c], Yansen Sun[d], Xin Qu[a,b,c], Rui Su[d], Mingyue Hu[a,b,c], Lei Chen[a,b,c], Yang Liu[a,b,c], Ming Gao[a,b,c,*], Jinghai Yang[a,b,c]

[a] *Key Laboratory of Functional Materials Physics and Chemistry of the Ministry of Education, Jilin Normal University, Changchun, 130103, PR China*
[b] *National Demonstration Centre for Experimental Physics Education, Jilin Normal University, Siping, 136000, PR China*
[c] *Key Laboratory of Preparation and Application of Environmental Friendly Materials, Jilin Normal University, Ministry of Education, Changchun, 130103, PR China*
[d] *Changchun Institute of Optics, Fine Mechanics and Physics, Chinese Academy of Sciences, Changchun, 130103, PR China*

ARTICLE INFO

Keywords:
Oxygen bidirectional strategy
SERS
MoS_2@ZnO
Ultrasensitive

ABSTRACT

Oxygen is one of the most abundant elements on earth, and even small amounts of oxygen can induce significant changes in material properties. In this study, we combined a non-oxide semiconductor molybdenum disulphide (MoS_2) with an oxide semiconductor zinc oxide (ZnO), thereby simultaneously obtaining oxygen vacancies and oxygen incorporations through a novel oxidation-assisted strategy. This strategy amplified interactions between semiconductor substrates and probe molecules and increased charge-transfer resonance, thereby substantially improving the surface-enhanced Raman spectroscopy (SERS) performance of semiconductor materials. The enhancement factor of MoS_2@ZnO was increased to a value comparable to that of traditional metals, enabling it to detect methylene blue with a limit of detection as low as 10^{-12} M. Additionally, a comparison sample (MoS_2@ZnS) was examined to confirm the unique enhancement effect of the proposed strategy for SERS. The effect of the proposed oxygen bidirectional strategy on the SERS performance of semiconductor substrates can provide new frontiers in the development of ultrasensitive semiconductor technologies.

1. Introduction

Surface-enhanced Raman spectroscopy (SERS) is a highly sensitive and nondestructive method that can be used to detect and identify compounds with monomolecular sensitivity [1–4]. SERS is promising for applications in the fields of medical diagnosis, biological imaging, chemical analysis, and environmental monitoring. Substrate materials are typically critical in SERS measurements due to large enhancement effects that can be achieved through two widely accepted mechanisms. The first mechanism is the electromagnetic mechanism (EM), which mainly originates from electric-field amplification induced by surface plasmon resonance. The EM generally contributes majorly to SERS enhancement, which is caused by noble metals, making single-molecule detection possible [5–8]. However, EM-based noble metals typically present three disadvantages—a complex manufacturing process, poor stability, and low biocompatibility—thereby restricting the practical applications of SERS [9]. The second mechanism is the chemical enhancement mechanism (CEM), which is induced by charge transfer (CT) between the SERS active material and probe molecule. Due to their excellent stability, biocompatibility, controllable bandgap, and geometry, semiconductor nanomaterials are superior to noble metals for their use as SERS active sensors [10,11]. However, the limit of detection (LOD) and Raman enhancement factor (EF) of semiconductor materials are inferior to those of noble-metal structures, which make them unsuitable for various applications. Therefore, the discovery of semiconductor substrates and development of novel strategies to enhance the SERS activity on a large scale by using low-cost methods are highly interesting [12].

In recent years, we have witnessed the development and advancement of semiconductor SERS substrates [13,14]. Among numerous methods for enhancing the SERS performance of semiconductor materials, introducing oxygen vacancies is a common strategy used for increasing the EF. Cong et al. reported that oxygen deficiencies in $WO_{2.72}$ can enhance Raman scattering [15]. Xi et al. reported that oxygen vacancy-rich MoO_2 exhibits an excellent sensitivity for detecting the trace amounts of dangerous chemicals [16]. However, this strategy is

---

[*] Corresponding author at: Key Laboratory of Functional Materials Physics and Chemistry of the Ministry of Education, and National Demonstration Centre for Experimental Physics Education, Jilin Normal University, Siping 136000, PR China.

E-mail address: gaomingphy@126.com (M. Gao).

https://doi.org/10.1016/j.snb.2020.128903
Received 5 May 2020; Received in revised form 19 August 2020; Accepted 12 September 2020

not suitable for non-oxide semiconductors; thus, new strategies are required for developing high-performance semiconductor SERS substrates. Oxygen incorporation is an excellent electronic modulation strategy for semiconductor nanomaterials and is the inverse process of introducing oxygen vacancies. This strategy can be employed to develop non-oxide semiconductors in the SERS substrate field. Zheng et al. reported an increased EF (1.4×10^5) and a reduced LOD (10^{-7} M) by incorporating oxygen in MoS_2 as a SERS substrate, oxygen incorporation was crucial for enhancing the SERS activity of the non-oxide semiconductor [17]. These results indicated that both oxygen vacancies (V_o) and oxygen incorporation (O_i) can substantially amplify the SERS signals of semiconductor substrates. Accordingly, oxygen vacancies combined with oxygen incorporation may yield high-performance SERS substrates.

In this paper, we propose a novel oxygen bidirectional strategy for optimising semiconductor SERS substrates. We combined the nanoflowers (NFs) of non-oxide semiconductor molybdenum disulphide (MoS_2) with the nanoparticles (NPs) of oxide semiconductor zinc oxide (ZnO) by employing a simple hydrothermal method. MoS_2, one of the most valuable 2D materials, presents properties such as a direct band gap and high carrier mobility, and its low-cost value and high chemical stability can help develop a cost-effective SERS technology [18,19]. Moreover, MoS_2 presents not only a suitable band gap and biocompatibility but also numerous active sites and appropriate surface roughness, which can be used to construct a better SERS-active substrate for SERS applications [20,21]. Additionally, SERS studies have been performed on ZnO because of its wide bandgap, growth economy, and diverse structure, which are the reasons why we selected ZnO as the ideal candidate for developing an oxygen bidirectional strategy [22–25]. Under external conditions, oxygen from ZnO was transferred to MoS_2; thus, oxygen vacancies were created in ZnO. Meanwhile, oxygen was introduced into MoS_2. This strategy experimentally demonstrated simple operation, low-cost, and excellent SERS performance. The semiconductor materials prepared using this unique strategy exhibited remarkable SERS activity with a high EF and low LOD of 1.13×10^6 and 10^{-12} M, respectively. The novel oxygen bidirectional strategy yielded a material that exhibited SERS sensitivity higher than all the reported pure semiconductor substrates.

2. Experimental

2.1. Synthesis of MoS_2 NFs

First, 0.5 *g* of $Na_2MoO_4 \cdot 2H_2O$ and 0.7 *g* of CH_4N_2S were mixed in 70 mL deionised water and vigorously stirred for 20 min to form a homogeneous and limpid solution. Subsequently, 0.5 *g* of $C_6H_8O_7 \cdot H_2O$ was weighed and dissolved in the homogeneous solution with stirring for 20 min until a homogeneous and clear solution was obtained again. This solution was then transferred into a 100 mL reaction kettle at 240 ℃ for 24 h. When the reaction kettle cooled to room temperature, the precipitate was repeated through centrifugation three times with ultrapure water and alcohol. Finally, it dried at 60℃ for 6 h to obtain the MoS_2 sample.

2.2. Synthesis of MoS_2@ZnO nanocomposites (NCs) with various contents of ZnO NPs

MoS_2@ZnO samples with the MoS_2 (Mo) and ZnO (Zn) molar ratios of 1:1, 1:4, and 1:8 were prepared. Three units of 0.1 *g* of MoS_2 were separately dispersed in 50 mL deionised water and sonicated for 30 min to obtain a homogeneous solution. Subsequently, $Zn(NO_3)_2 \cdot 6H_2O$ (0.1860, 0.7438, or 1.4876 *g*) and $C_6H_{12}N_4$ (0.0443, 0.1752, or 0.3504 *g*) were separately dispersed in the three units of this solution, and then 1, 4, or 8 mL of ammonia water was added to these three mixed solutions and the resulting solutions were stirred for 20 min. Afterwards, we transferred the solutions into a water bath pot maintained at a constant temperature of 60 ℃, and heated it for 3 h. The obtained samples were separated through centrifugation, washed with ultrapure water and ethanol, finally dried at 60 ℃ for 6 h, and denoted as '$MoS_2@ZnO_{1:X}$' (X = 1, 4, or 8).

2.3. Synthesis of MoS_2@ZnS NCs

To confirm the unique enhancement effect of the oxygen bidirectional strategy for SERS, a comparison sample MoS_2@ZnS (non-oxide semiconductor - non-oxide semiconductor) was prepared. Primarily, prepared MoS_2 (50 mg), $Zn(CH_3COO)_2$ (229 mg), and CH_4N_2S (100 mg) were added into 50 mL deionised water. After 30 min stirring, this solution was transferred into a 100 mL reaction kettle and heated at 150 °C for 8 h. After the reaction kettle naturally cooled to room temperature, the obtained precipitate was separated using centrifugation, washed with ultrapure water and ethanol, and dried at 60 °C for 6 h to obtain MoS_2@ZnS.

2.4. Characterisation

The morphology of $MoS_2@ZnO_{1:X}$ was characterised using scanning electron microscopy (SEM, JSM-7800 F) and transmission electron microscopy (TEM, JEM-2100 h). The structure quality of the samples was analyzed using X-ray diffraction (XRD, Rigaku D/Max 3C) and X-ray photoelectron spectroscopy (XPS, Thermo ESCALAB 250). Ultraviolet (UV)-vis absorption spectra were measured at room temperature with a Hitachi U-3600 spectrophotometer (Shimadzu, Japan). UV photoelectron spectroscopy (UPS) analysis was performed using an ESCALAB 250Xi UPS system (thermo Fisher scientific). The Brunauer–Emmett–-Teller (BET) specific area was measured through the nitrogen adsorption/desorption isotherms by employing a NOVA2200e instrument (TriStar II 3020). SERS signals were detected using a Renishaw in through a Raman system under a 514.5-nm Ar^+ ion laser.

2.5. SERS experiments of methylene blue (MB)

The SERS activity of the samples was investigated using MB, a common active probe molecule. The prepared samples (3 mg) were immersed in a 10^{-3}–10^{-12} M MB ethanol solution and continuously shaken for 12 h to ensure complete adsorption. Similarly, 3 mg of MoS_2@ZnS powders were immersed in a 10^{-3} M MB ethanol solution and shaken for 12 h. All SERS spectra were acquired using Renishaw inVia Raman system under an excitation laser of 514.5 nm for 30 s with 1 scan every spectrum. The laser power was 40 mW, attenuating 1%.

3. Results and discussion

3.1. Structure and morphology of $MoS_2@ZnO_{1:X}$

By manipulating the ZnO amount, $MoS_2@ZnO_{1:X}$ was successfully prepared (Fig. 1). The self-assemble process was described in detail in our previous study [26]. MoS_2 are composed of many thin folds in different directions with a diameter of approximately 2–3 μm (Fig. 1a). By changing the ZnO amount, $MoS_2@ZnO_{1:X}$ was successfully obtained using a two-step hydrothermal method. Fig. 1b–d shows that the morphology of ZnO grown in situ on the MoS_2 surface was affected by the molar ratios of Mo and Zn. Fig. 1b shows the morphology of the $MoS_2@ZnO_{1:1}$ composite with crumpled and entangled nanosheets. Only a small amount of ZnO NPs were dotted on the MoS_2 NFs surface, which exhibited a small effect on the overall morphology. Fig. 1c shows $MoS_2@ZnO_{1:4}$ with uniformly and densely grown ZnO NPs on the MoS_2 NFs surface. With an increase in the ZnO amount, an increasing amount of ZnO accumulated on MoS_2, which eventually became a microsphere completely wrapped with ZnO NPs (Fig. 1d). To more clearly indicate the distribution of ZnO on the MoS_2 surface, Fig. 1e–g shows that MoS_2 were modified with different contents of ZnO NPs (red area). Fig. 1h

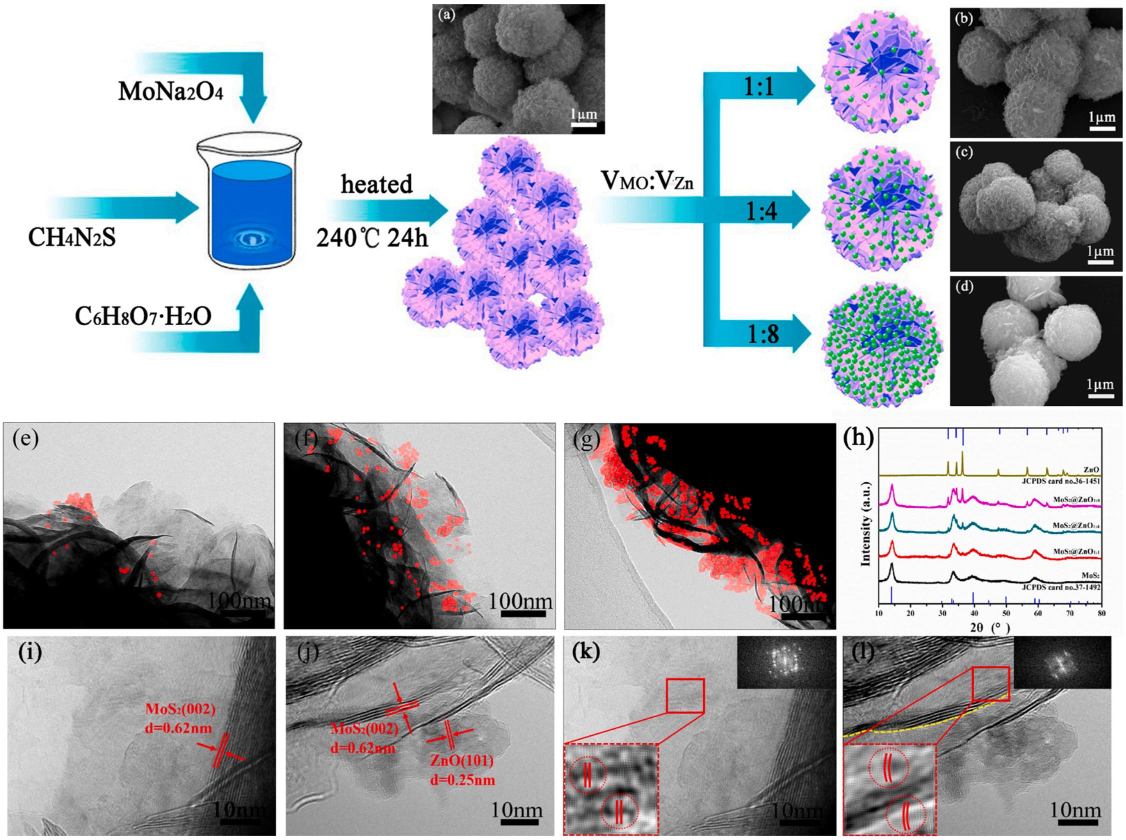

Fig. 1. Schematic illustrations of the hydrothermal synthesis procedure to obtain $MoS_2@ZnO_{1:X}$ NCs. (a-d) SEM images of MoS_2, $MoS_2@ZnO_{1:1}$, $MoS_2@ZnO_{1:4}$, $MoS_2@ZnO_{1:8}$, respectively. (e-g) TEM images of $MoS_2@ZnO_{1:1}$, $MoS_2@ZnO_{1:4}$, $MoS_2@ZnO_{1:8}$, respectively. (h) XRD patterns of MoS_2 NFs, ZnO NPs, $MoS_2@ZnO_{1:X}$ NCs. (i) HRTEM images of MoS_2. (j) HRTEM images of $MoS_2@ZnO_{1:4}$ sample. (k) The lattice image of the rectangle region (MoS_2) was further analyzed by the back and forth FFT. (l) The lattice image of the rectangle region ($MoS_2@ZnO_{1:4}$) was further analyzed by the back and forth FFT.

shows the XRD patterns of MoS_2 NFs, ZnO NPs, $MoS_2@ZnO_{1:1}$ NCs, $MoS_2@ZnO_{1:4}$ NCs, and $MoS_2@ZnO_{1:8}$ NCs. The XRD pattern of MoS_2 NFs sample is similar to that of the pristine 2H–MoS_2 (JCPDS card no.37–1492). Furthermore, ZnO diffraction peaks correspond to the hexagonal wurtzite structure (JCPDS card no. 36-1451). The peak strength of ZnO increased with an increase in the ZnO content on the MoS_2 surface. Fig. 1i–j presents the results of the high-resolution TEM (HRTEM) analysis. Obvious lattice lines indicated suitable crystallisation and agree well with the hexagonal MoS_2 structure with the spacing of 0.62 nm, which corresponds to the (002) crystallographic plane [27]. The lattice spacing of 0.25 nm is consistent with the (101) crystallographic plane of hexagonal ZnO [28]. The HRTEM image of MoS_2 (Fig. 1i) was captured for analysis by using back and forth fast Fourier transformation (FFT) (Fig. 1k). The crystal lattice of pure MoS_2 was straight, and no bending was observed. By contrast, obvious lattice bending was observed at the interface between ZnO and MoS_2 (Fig. 1l) because oxygen in ZnO was incorporated into the crystal lattice of MoS_2 and Mo atoms were oxidised along the edge planes of MoS_2 crystals [29]. In these twisty areas, local electronic properties changed observably compared with electronic properties in the undistorted regions, possibly affecting the CT efficiency and amplifying molecular polarisation, eventually leading to an increase in SERS signals.

3.2. SERS activity of $MoS_2@ZnO_{1:X}$

To confirm this conjecture, MB was used to examine the SERS activity of the pure MoS_2 and $MoS_2@ZnO_{1:X}$ samples. These samples showed considerably large differences in SERS sensitivity. In Fig. 2a, the common seven characteristic peaks of MB (10^{-3} M), 448, 501, 770, 1156, 1303, 1397, and 1626 cm^{-1}, are marked. The strongest peak at 1626 cm^{-1} is assigned to the ring stretching of C—C, the peaks at 448 and 501 cm^{-1} may originate from the skeletal deformation of C—N—C, the peaks at 770 and 1156 cm^{-1} correspond to the in-plane bending of C—H, the peak at 1303 cm^{-1} can be assigned to the in-plane ring deformation of C—H, and the peak at 1397 cm^{-1} is attributed to the symmetrical stretching of C—N [30]. To clearly show the change in the intensity with respect to ZnO concentrations, the SERS intensity of 1397 and 1626 cm^{-1} was plotted (Fig. 2b). The SERS intensity initially increased with an increasing concentration of ZnO, reaching a maximum for $MoS_2@ZnO_{1:4}$ and then showed a decreasing trend. To scientifically compare the SERS performance of these samples, EF values were calculated. The EF was roughly estimated using the following equation [31,17]:$EF=(I_{SERS}/I_{Raman})(N_{Raman}/N_{SERS})$

where I_{SERS} and I_{Raman} are the integrated of the SERS and Raman scattering spectra, respectively, for MB with and without SERS substrate under the same test condition (Fig. 2c); N_{SERS} and N_{Raman} are the numbers of the MB molecules probed with and without substrate materials, respectively. The EF was estimated by assuming that a MB monolayer film sufficiently covered the substrate surface. The detailed calculation process is shown in Supporting Information. For $MoS_2@ZnO_{1:4}$, the EF can reach as high as 1.13×10^6 when evaluated as the band of 1626 cm^{-1}, and to the best of our knowledge, this EF is better than the EF of the reported semiconductor nanomaterials [32,33]. Furthermore, even with $MoS_2@ZnO_{1:1}$ and $MoS_2@ZnO_{1:8}$, the EFs can reach 5.28×10^5 and 7.08×10^5, respectively. These results further revealed that the SERS activity of $MoS_2@ZnO_{1:X}$ samples is comparable to or better than that of noble metals. Fig. 2b shows that the EF trend is consistent with the Raman intensity. Even small amounts of oxygen induced a substantial change in the SERS performance of these samples.

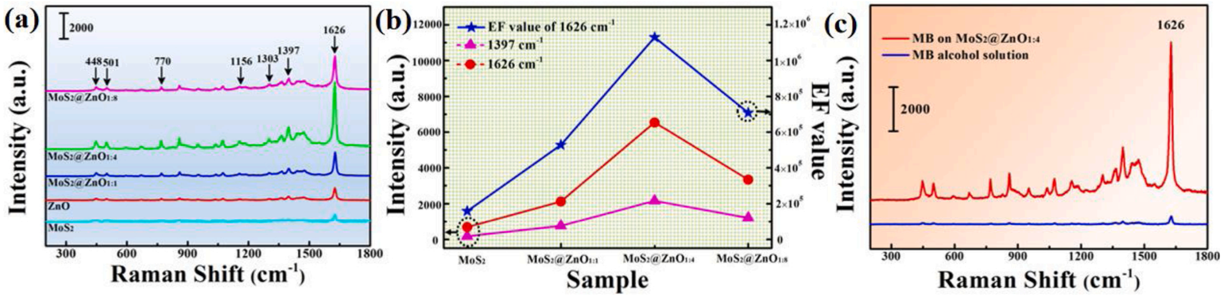

Fig. 2. (a) SERS spectra of MB absorbed on MoS_2, ZnO and $MoS_2@ZnO_{1:X}$ samples. (b) A plot of the SERS intensity of the 1397 and 1626 cm^{-1} versus MoS_2 and $MoS_2@ZnO_{1:X}$ samples, and the EF values of different samples. (c) SERS spectra of MB (10^{-3} M) absorbed on $MoS_2@ZnO_{1:4}$ substrate (red line) and MB alcohol solution (blue line). **(For interpretation of the references to colour in this figure legend, the reader is referred to the web version of this article).**

3.3. Analysis of SERS mechanism

The EF of traditional semiconductor substrates is usually in the range of 10^1–10^3, which is considerably lower than that of $MoS_2@ZnO_{1:4}$ (10^6). Thus, an in-depth mechanism study must be performed. The XPS analysis was conducted to further demonstrate the bidirectional action of oxygen. Fig. 3a shows the survey spectrum of MoS_2 and $MoS_2@ZnO_{1:X}$, all elements of which can be easily indexed. The spectrum recorded before recombination exhibits photoelectron signals attributable to the photoemission peaks of Mo $3d_{3/2}$, Mo $3d_{5/2}$, S $2p_{1/2}$, and S $2p_{3/2}$ appearing at 231.2, 228.1, 162.7, and 161.5 eV, respectively. When ZnO successfully recombined with MoS_2, the peaks of O 1s, Zn $2p_{1/2}$, and Zn $2p_{3/2}$ appeared with the binding energies of 1044.0, 1021.0, and 531.8 eV, respectively. The peak intensity of these three peaks showed an increasing trend with an increase in the ZnO content [34]. Fig. 3b presents the wide and asymmetric XPS peak of O 1s of $MoS_2@ZnO_{1:4}$, the peak at 530.68 eV is assigned to the oxygen in the lattice (Zn–O and Mo–O), which is caused by oxidation that resulted in O^{2-} in ZnO combined with Mo^{4+} to form Mo–O bonds. The peak at the binding energy of 531.4 eV is caused by O^{2-} ions present in oxygen vacancy areas in ZnO. The centred peak at 532.0 eV corresponds to surface OH^- groups, adsorbed or dissociated oxygen on the surface of MoS_2 and ZnO [35]. The percentage of defect oxygen calculated was 24.7 %. Thus, the contribution of defect oxygen (oxygen-vacant ZnO) to the CT degree was 10.6 % (detailed calculation is presented in Supporting Information) [36]. Fig. 3c shows the XPS spectra of Mo for the $MoS_2@ZnO_{1:1}$,

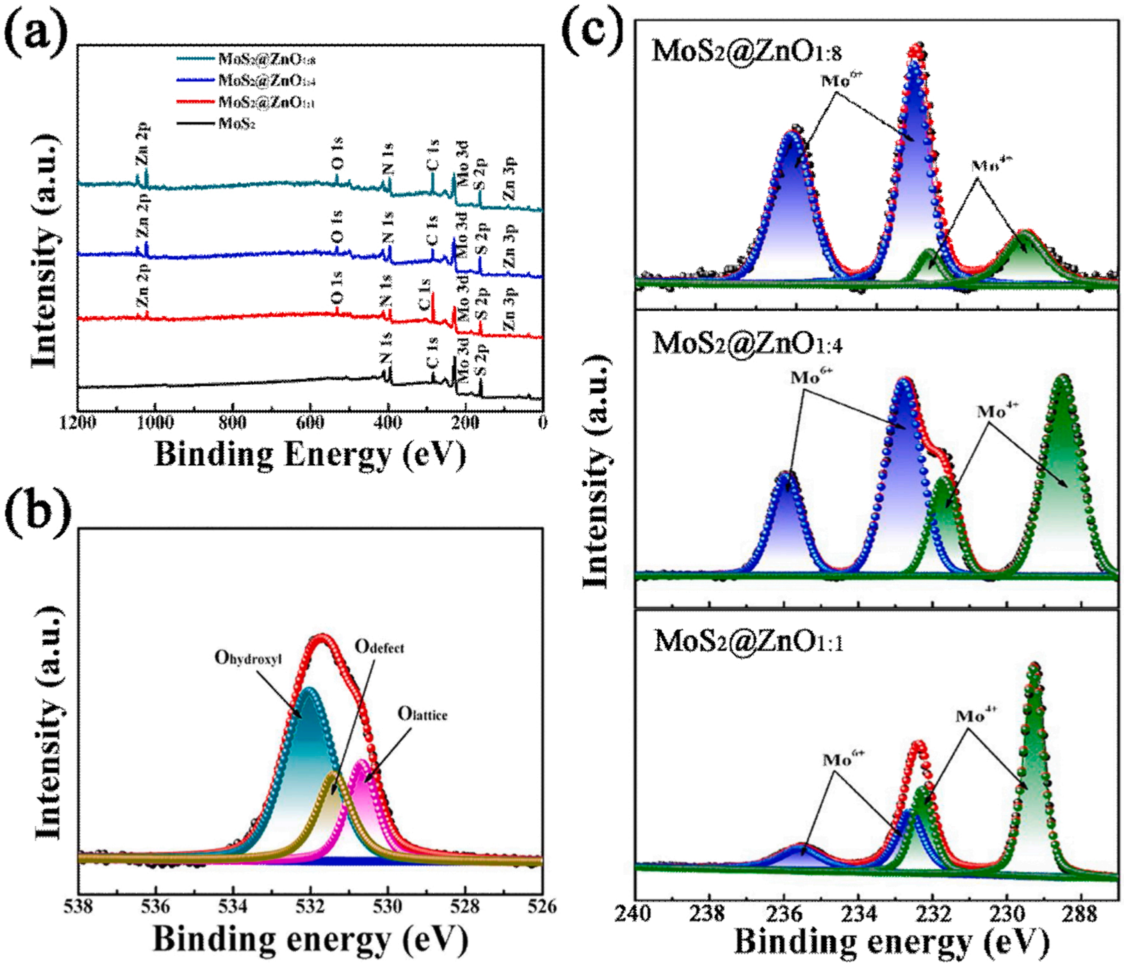

Fig. 3. XPS for (a) Survey spectrum (MoS_2 and $MoS_2@ZnO_{1:X}$); (b) The XPS spectra of O-1 s of $MoS_2@ZnO_{1:4}$. (c)The XPS spectra of Mo 3d of $MoS_2@ZnO_{1:X}$.

$MoS_2@ZnO_{1:4}$, and $MoS_2@ZnO_{1:8}$ samples. For $MoS_2@ZnO_{1:1}$, two Mo $3d_{5/2}$ and Mo $3d_{3/2}$ of Mo^{4+} signals appeared at the binding energy of 229.2 and 232.2 eV, other two weak shoulder peaks at 232.6 and 235.6 eV can correspond to Mo^{6+}, and only a small portion of Mo^{4+} was oxidised to Mo^{6+} during the reaction [16]. According to the peak areas, the concentration of Mo^{6+} in $MoS_2@ZnO_{1:4}$ considerably increased. In addition, the electronegativity of oxygen was stronger than that of sulphur, which indicated that oxidation increased mutual repulsion between adjacent layers. This repulsion caused a large increase in the spacing between the adjacent layers of MoS_2, which ultimately led to Mo peak broadening. However, when the ZnO concentration was considerably high, the resultant ZnO tended to self-nucleate and grow into independent ZnO particles. These ZnO particles were wrapped on the MoS_2 surface, so that most Mo^{4+} can oxidise to Mo^{6+}, which eventually resulted the low concentration of Mo^{4+}.

The XPS results indicated that when the non-oxide semiconductor (MoS_2) combined with oxide semiconductor (ZnO), the oxygen ions in the ZnO doped into MoS_2 under the action of external energy (thermal energy, light energy), while oxygen vacancies generated in ZnO simultaneously. To investigate the contribution of $MoS_2@ZnO_{1:4}$ to oxygen vacancies, Fig. 4a presents the photoluminescence (PL) spectra of pure ZnO and $MoS_2@ZnO_{1:4}$. The deep level emission (DLE) of ZnO was caused by an electronic transition from defect-associated trap states, such as oxygen vacancies [[37]]. The DLE peak intensity of $MoS_2@ZnO_{1:4}$ was stronger than that of ZnO, which indicated that after combination, MoS_2 generated more oxygen vacancies in ZnO. The oxygen vacancies caused by combining with MoS_2 generated new energy levels under the conduction band as an electron trap, which inhibited photoexcited charge recombination induced by photo excitation [38]. This phenomenon played an irreplaceable role in facilitating efficient CT processes between semiconductor materials and the matching energy levels of the adsorbed MB molecules, resulting in the further enhancement of SERS signals.

To understand the effect of oxygen ions on MoS_2, both the pure MoS_2 and oxygen-doped MoS_2 systems were investigated through first-principle density functional theory (DFT) simulation (Fig. 4b, c) (simulation details are provided in Supporting Information). The final simulation results confirmed that the incorporation of oxygen in MoS_2 NFs can lead to a narrow bandgap and improve intrinsic conductivity, which is in strong agreement with the study of Zheng [17]. The bandgap reduction can be ascribed to the enhanced hybridisation of the p-orbital of S and D-orbital of Mo when incorporating oxygen. Compared with the valence band (VB) position of pure MoS_2, partially oxygen-incorporated MoS_2 exhibited obviously downward orientation, which made transition energy form VB to lowest unoccupied molecular orbital (LUMO) to be closer to excitation laser energy; thus, a stronger CT resonance was achieved for oxygen-incorporated MoS_2. The CT contribution of oxygen-incorporated MoS_2 was 32.4 % (Supporting Information). In addition, the UV–vis and UPS spectra were used to measure the actual band structure of ZnO, MoS_2, and $MoS_2@ZnO$ heterostructures (Fig. S2 and S3, Supporting Information). According to the measurements and calculation results, Fig. 4d presents the charge transfer mechanism.

Although CT resonance is vital for higher Raman enhancement on oxygen vacancies in oxygen-vacant ZnO and oxygen-incorporated MoS_2, other factors in this system also make irreplaceable contributions. The sulphur atoms of MoS_2 are present on the surface, and the polarity of polar-covalent Mo–S bonds is vertical to MoS_2 surface; therefore, interface dipole-dipole coupling might simultaneously occur with charge transfer, which could induce effective Raman enhancement [39, 40].

The last factor to consider is the specific surface area. The larger is the specific surface area, the more are the probe molecules adsorbed, which ultimately leads to stronger Raman signals. The BET specific area and pore volume of these samples were investigated through nitrogen adsorption–desorption isotherms. Fig. 4e–h shows N_2 gas adsorption–desorption isotherms for the samples, and the insets represent pore volume distribution curves. The BET surface area of pure MoS_2, $MoS_2@ZnO_{1:1}$, $MoS_2@ZnO_{1:4}$, and $MoS_2@ZnO_{1:8}$ obtained from isotherms was 3.795, 8.676, 14.785, and 8.030 $m^2\ g^{-1}$, respectively. The BET specific surface areas of composites tended to be larger initially and then to decrease because when the ZnO load was low, ZnO NPs were randomly distributed on MoS_2 NF folds, resulting in higher roughness (the specific surface area of the composite samples was higher than that of pure MoS_2) and an increased specific area from 3.795 to 8.676 $m^2\ g^{-1}$. $MoS_2@ZnO_{1:4}$ resulted in the highest specific area, which can be attributed to the layered structure that provided an appropriate surface for dispersion of ZnO NP dispersion, thereby providing more reaction sites for MB adsorption. However, when ZnO NPs were overloaded, they were converged and coated on the MoS_2 surface. All the synthesised $MoS_2@ZnO_{1:8}$ samples were micro-spherical with a diameter approximately 3 μm, which reduced the composite roughness; thus, the specific surface area decreased. The design and synthesis of $MoS_2@ZnO_{1:4}$ with both oxygen vacancies and incorporations is highly conducive to the adsorption of probe molecules.

To verify the effect of oxygen bidirectional action on improving the SERS activity of non-oxide semiconductor-oxide semiconductor

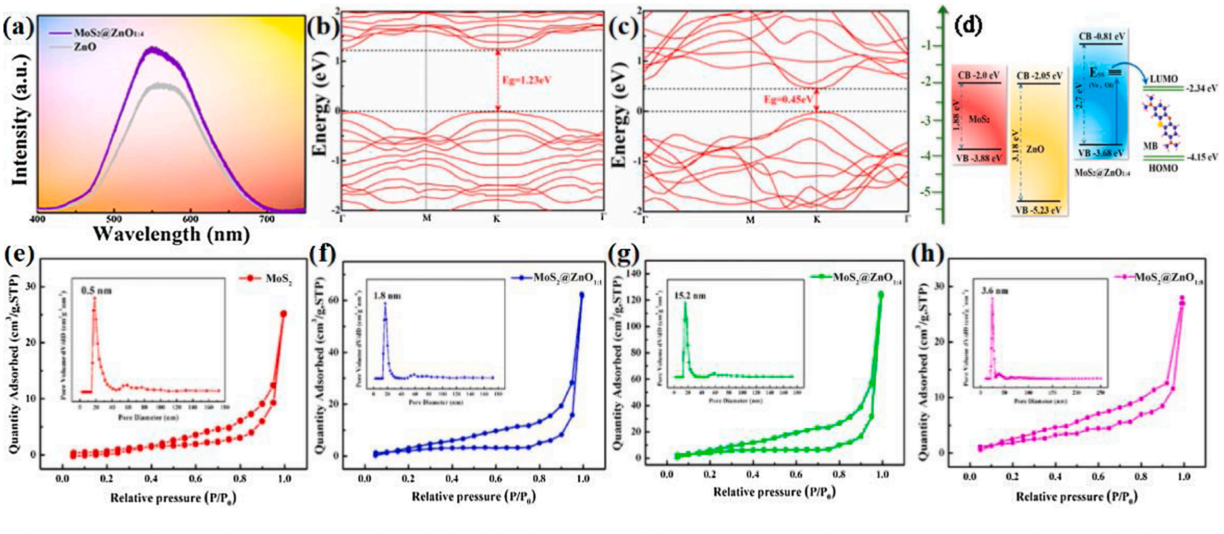

Fig. 4. (a) The PL spectra of ZnO and $MoS_2@ZnO_{1:4}$; The calculated band structures of (b) pristine MoS_2 and (c) oxygen-incorporated MoS_2; (d)Schematic diagram of the enhancement mechanism; N_2 adsorption-desorption isotherms and the pore size distribution (the inset) of (e) MoS_2, (f) $MoS_2@ZnO_{1:1}$, (g) $MoS_2@ZnO_{1:4}$, (h) $MoS_2@ZnO_{1:8}$.

composite materials, several spectra were investigated under the same conditions for another crucial wide bandgap non-oxide semiconductor of ZnS material. Fig. 5a presents the XRD characteristics of the MoS_2@ZnS sample for the molar ratio of Mo (MoS_2) and Zn (ZnS) was 1:4; no impurity peaks appeared and these diffraction peaks were assigned to 2H–MoS_2 (JCPDS No.37–1492) and sphalerite ZnS (JCPDS No.05−0566). The morphology of MoS_2@ZnS is similar to that of MoS_2@ZnO, both of which are NPs attached on NFs (Fig. 5b and c). MoS_2@ZnS exhibits the BET specific surface area of 15.6 m^2/g, which is considerably close to that of MoS_2@$ZnO_{1:4}$ (14.785 m^2/g) (Fig. 5d). Therefore, the effect of the specific surface area on the enhanced Raman signal can be ignored. Moreover, the XPS spectrum of MoS_2@ZnS (Fig. 5e and f) indicated an absence of O 1S and Mo^{6+}, which further confirmed that the oxygen bidirectional strategy did not influence the SERS activity of MoS_2@ZnS. Fig. 5g shows the comparison of SERS spectra between MB collected on MoS_2@$ZnO_{1:4}$ and MoS_2@ZnS. For the MoS_2@ZnS samples, the average SERS intensity at approximately 1626 cm^{-1} is substantially lower than that for MoS_2@$ZnO_{1:4}$. The EF for MoS_2@ZnS can reach as high as 3.97×10^4. By contrast, the estimated EF value of MoS_2@$ZnO_{1:4}$ is hundred times larger than that of the MoS_2@ZnS sample. This finding further confirmed the extremely vital contribution of oxygen in enhancing the SERS performance of composite semiconductors.

MB is often used as a fungicide and an antidote in the aquaculture. However, studies have shown that MB is highly toxic, teratogenic, carcinogenic, and mutagenic. Due to its extensive use and abuse, MB has caused some toxicity and side effects in aquaculture animals [41]. Therefore, the trace detection of MB molecules is crucial. Fig. 6a presents the concentration-dependent SERS spectra of MoS_2/$ZnO_{1:4}$ of MB (10^{-3}–10^{-12} M). With the gradual dilution of the MB solution, the intensity of the main characteristic Raman peak decreased. Although the concentration of the MB solution decreased to 10^{-12} M, the Raman peak at 1626 cm^{-1} was visible (inset of Fig. 6a), which indicated that the detection limit can reach 10^{-12} M. This result is substantially lower than the concentration of 0.4 mg/kg (1.07×10^{-6} M) set by the EU as a disinfectant. To the best of our knowledge, the SERS performance of the MoS_2/$ZnO_{1:4}$ sample is significantly superior to that of most previous semiconductor SERS substrates (Fig. 6b) [42–47] and to the comparison sample (MoS_2@ZnS) (Fig. 5h). Fig. 6c shows the linear correlation between the SERS intensity of the MoS_2@$ZnO_{1:4}$ system and MB concentration. The calibrated linear regression equation at 1626 cm^{-1} can be described as $\log(I_{1626}) = (528 \pm 22)\log C_{MB} + (6165 \pm 172)$, and for this regression model, the squared correlation coefficient (R^2) is as high as 0.9696, which can provide a reliable basis for the determination of MB residue in both qualitative and quantitative analyses.

In actual applications, in addition to the SERS activity, the stability and uniformity of substrates are problems that must be considered. Almost no change was observed in the SERS spectra of substrate materials at different storage times (0–3 month) (Fig. 6d). This result indicated that the MoS_2@$ZnO_{1:4}$ substrate presents extremely high stability. Fig. 6e presents a 3D waterfall plotted using the SERS signals from 20 random positions on the MoS_2@$ZnO_{1:4}$ substrate. The estimated relative standard deviation for the 1626 cm^{-1} peak was 11.3 % (Fig. 6f). Our results showed that the substrate presents good uniformity. The outstanding sensitivity, excellent reproducibility, and remarkable uniformity further demonstrated the practical use of MoS_2@$ZnO_{1:4}$ substrates.

4. Conclusion

We proposed an effective strategy for the first time: oxygen bidirectional strategy, to greatly ameliorate the defects of semiconductors to be used as SERS substrates. During the recombination of the oxide semiconductor (ZnO) and non-oxide semiconductor (MoS_2), a part of oxygen escapes from ZnO into MoS_2 as an active centre, which results in the simultaneous oxygen vacancies and oxygen incorporation phenomenon. The MoS_2@$ZnO_{1:4}$ substrate exhibited a remarkable SERS sensitivity with an EF of 1.13×10^6 and a considerably LOD of 10^{-12} M for the MB molecules, which is higher than that of the most semiconductor SERS substrates and is comparable to that of traditional noble metals. The unique oxidation-assisted strategy not only offers crucial method for the realisation of semiconductor substrate with a high SERS activity but also provides an avenue for wide applications of semiconductor SERS such as food safety, chemical analysis, bioscience, material science, and biological imaging.

CRediT authorship contribution statement

Yingnan Quan: Investigation, Data curation, Writing - original draft. **Jiacheng Yao:** Conceptualization, Methodology. **Yansen Sun:** Methodology, Resources. **Xin Qu:** Software. **Rui Su:** Investigation, Visualization. **Mingyue Hu:** Investigation, Visualization. **Lei Chen:** Formal analysis. **Yang Liu:** Supervision. **Ming Gao:** Writing - review & editing, Funding acquisition. **Jinghai Yang:** Project administration.

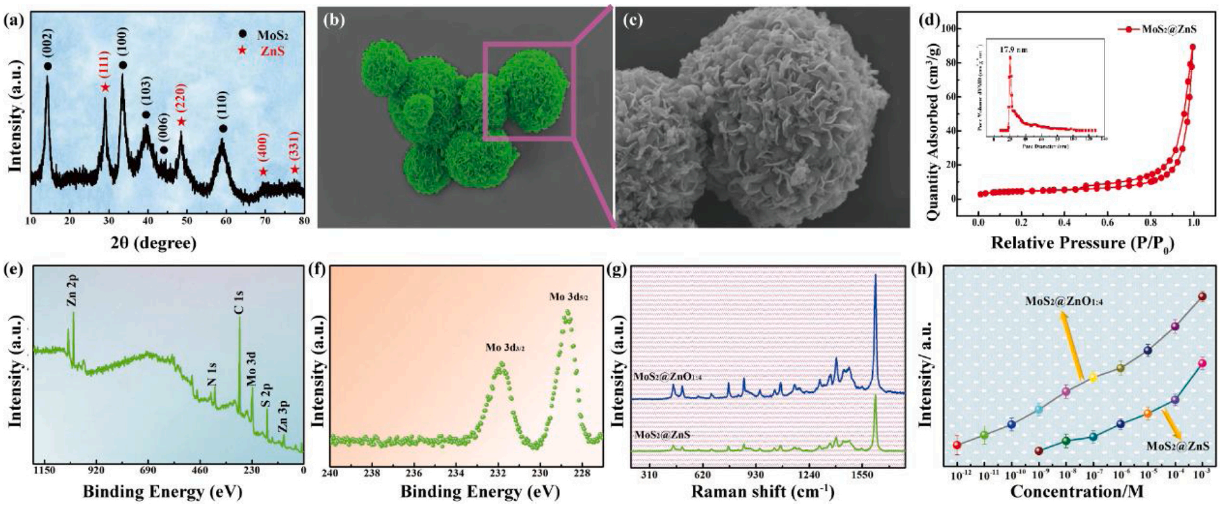

Fig. 5. (a) The XRD pattern of the MoS_2/ZnS nanocomposites. (b-c) The SEM images of the MoS_2/ZnS nanocomposites under different magnification. (d) N_2 adsorption-desorption isotherms and the pore size distribution (the inset) of MoS_2/ZnS. **(**e**)** XPS for Survey spectrum of MoS_2@ZnS. (f) The XPS spectra of Mo 3d of MoS_2@ZnS. (g) SERS spectra of MB (1.0×10^{-3} M) on the MoS_2/$ZnO_{1:4}$ and MoS_2/ZnS samples. (h) The corresponding Raman intensity variations at 1626 cm^{-1} with different concentrations of MB on two substrates.

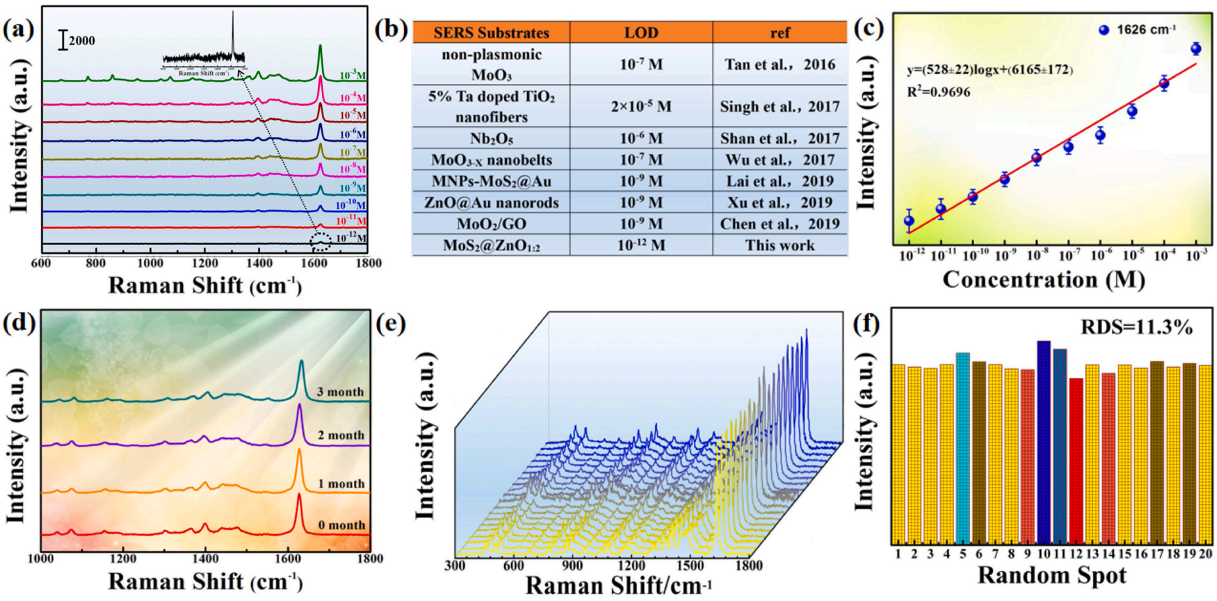

SERS Substrates	LOD	ref
non-plasmonic MoO_3	10^{-7} M	Tan et al.，2016
5% Ta doped TiO_2 nanofibers	2×10^{-5} M	Singh et al.，2017
Nb_2O_5	10^{-6} M	Shan et al.，2017
MoO_{3-X} nanobelts	10^{-7} M	Wu et al.，2017
MNPs-MoS_2@Au	10^{-9} M	Lai et al.，2019
ZnO@Au nanorods	10^{-9} M	Xu et al.，2019
MoO_2/GO	10^{-9} M	Chen et al.，2019
MoS_2@$ZnO_{1:2}$	10^{-12} M	This work

Fig. 6. (a)SERS spectra of MoS_2@$ZnO_{1:4}$ NCs incubated with MB aqueous solution at various concentration and the inset is SERS spectra of MB aqueous solution at 10^{-12} M; (b) the table of SERS detection limits for different substrates using MB as probe molecule; (c) the calibration curve for MB at 1626 cm^{-1}; (d) SERS spectra of MB aqueous solution at 10^{-9} M based on MoS_2@$ZnO_{1:4}$ collected at different shelf time; (e) a series of SERS spectra of MB in water samples collected on 20 randomly selected spots of the MoS_2@$ZnO_{1:4}$ substrate; (f) SERS intensity of MB at 1626 cm^{-1} of the 20 SERS spectra.

Declaration of Competing Interest

The authors declare no competing financial interest.

Acknowledgements

This work was supported by the National Natural Science Foundation of China (No. 61675090 and 21776110); National Youth Program Foundation of China (No. 61405072 and 61704065); the Program for the Development of Science and Technology Jilin Province (Grant Numbers 20200201022JC, 20190103002JH and 20180520179JH, 20160101287JC and 20180520179JH); the Thirteenth Five-Year Program for Science and Technology ofEducation Department of Jilin Province (Grant Numbers JJKH20190550KJ).

Appendix A. Supplementary data

Supplementary material related to this article can be found, in the online version, at doi:https://doi.org/10.1016/j.snb.2020.128903.

References

[1] R.X. Gao, Y.J. Zhang, F. Zhang, S. Guo, Y.X. Wang, L. Chen, J.H. Yang, SERS polarization-dependent effects for an ordered 3D plasmonic tilted silver nanorod array, Nanoscale 10 (2018) 8106–8114.

[2] R.K. Gao, X.F. Song, C.B. Zhan, C.G. Weng, S. Cheng, K. Guo, N. Ma, H.F. Chang, Z. Y. Guo, L.B. Luo, L.D. Yu, Light trapping induced flexible wrinkled nanocone SERS substrate for highly sensitive explosive detection, Sensor. Actuat. B-Chem. 314 (2020), 128081.

[3] Y.J. Zhang, H.H. Sun, R.X. Gao, F. Zhang, A.N. Zhu, L. Chen, Y.X. Wang, Facile SERS-active chip (PS@Ag/SiO_2/Ag) for the determination of HCC biomarker, Sensor. Actuat. B-Chem. 272 (2018) 34–42.

[4] Y.N. Quan, J.C. Yao, S. Yang, L. Chen, Y. Liu, J.H. Lang, H.Q. Zeng, J.H. Yang, M. Gao, Detect, remove and re-use: sensing and degradation pesticides via 3D tilted ZMRs/Ag arrays, J. Hazad. Mater. 391 (2020), 122222.

[5] X.Y. Zhang, D.L. Han, N. Ma, R.X. Gao, A.N. Zhu, S. Guo, Y.J. Zhang, Y.X. Wang, J. H. Yang, L. Chen, Carrier density-dependent localized surface plasmon resonance and charge transfer observed by controllable semiconductor content, J. Phys. Chem. Lett. 9 (2018) 6047–6051.

[6] V. Živanovi, Z. Kochovski, C. Arenz, Y. Lu, J. Kneipp, SERS and Cryo-EM directly reveal different liposome structures during interaction with gold nanoparticles, J. Phys. Chem. Lett. 9 (2018) 6767–6772.

[7] P. Singh, T.A.F. Koenig, A. Jaiswal, NIR-active plasmonic gold nanocapsules synthesized using thermally induced seed twinning for surface-enhanced raman scattering applications, ACS Appl. Mater. Inter. 10 (2018) 39380–39390.

[8] R. Botta, P. Eiamchai, M. Horprathum, S. Limwichean, C. Chananonnawathorn, V. Patthanasettakul, R. Maezono, A. Jomphoak, N. Nuntawong, 3D structured laser engraves decorated with gold nanoparticle SERS chips for paraquat herbicide detection in environments, Sensor. Actuat. B-Chem. 304 (2020), 127327.

[9] I. Alessandri, J.R. Lombardi, NIR-active plasmonic gold nanocapsules synthesized using thermally induced seed twinning for surface-enhanced raman scattering applications, Chem. Rev. 116 (2016) 14921–14981.

[10] X.T. Wang, W.X. Shi, S.X. Wang, H.W. Zhao, J. Lin, Z. Yang, M. Chen, L. Guo, Two-dimensional amorphous TiO2 nanosheets enabling high-efficiency photoinduced charge transfer for excellent SERS activity, J. Am. Chem. Soc. 141 (2019) 5856–5862.

[11] J. Lin, Y. Shang, X.X. Li, J. Yu, X.T. Wang, L. Guo, Ultrasensitive SERS detection by defect engineering on single Cu2O superstructure particle, Adv. Mater. 19 (2017), 1604797.

[12] I. Alessandri, Enhancing raman scattering without plasmons: unprecedented sensitivity achieved by TiO2 shell-based resonators, J. Am. Chem. Soc. 135 (2013) 5541–5544.

[13] S. Cong, Y.Y. Yuan, Z.G. Chen, J.Y. Hou, M. Yang, Y.L. Su, Y.Y. Zhang, L. Li, Q. W. Li, F.X. Geng, Z.G. Zhao, Noble metal-comparable SERS enhancement from semiconducting metal oxides by making oxygen vacancies, Nat. Commun. 6 (2015) 7800.

[14] X. Zhao, W.Z. Wang, Y.J. Liang, J.L. Fu, M. Zhu, H.L. Shi, S.J. Lei, C.J. Tao, Visible-light-driven charge transfer to significantly improve surface-enhanced Raman scattering (SERS) activity of self-cleaning TiO_2/Au nanowire arrays as highly sensitive and recyclable SERS sensor, Sensor. Actuat. B-Chem. 279 (2019) 313–319.

[15] S. Cong, Y.Y. Tian, Q.W. Li, Z.G. Zhao, F.X. Geng, Single-crystalline tungsten oxide quantum dots for fast pseudocapacitor and electrochromic applications, Adv. Mater. 26 (2014) 4260–4267.

[16] Q.Q. Zhang, X.S. Li, Q. Ma, Q. Zhang, H. Bai, W.C. Yi, J.Y. Liu, J. Han, G.C. Xi, A metallic molybdenum dioxide with high stability for surface enhanced Raman spectroscopy, Nat. Commun. 8 (2017) 14903.

[17] Z.H. Zheng, S. Cong, W.B. Gong, J.N. Xuan, G.H. Li, W.B. Lu, F.X. Geng, Z.G. Zhao, Semiconductor SERS enhancement enabled by oxygen incorporation, Nat. Commun. 8 (2017) 1993.

[18] D. Kathiravan, B.R. Huang, A. Saravanan, A. Prasannan, P.D. Hong, Highly enhanced hydrogen sensing properties of sericin-induced exfoliated MoS_2 nanosheets at room temperature, Sensor. Actuat. B-Chem. 279 (2019) 138–147.

[19] H. Li, Q. Zhang, C.C.R. Yap, B.K. Tay, T.H.T. Edwin, A. Olivier, D. Baillargeat, From bulk to monolayer MoS2: evolution of raman scattering, Adv. Funct. Mater. 22 (2012) 1385–1390.

[20] S. Su, C. Zhang, L.H. Yuwen, J. Chao, X.L. Zuo, X.F. Liu, C.Y. Song, C.H. Fan, L. H. Wang, Creating SERS hot spots on MoS2 nanosheets with in situ grown gold nanoparticles, ACS Appl. Mater. Inter. 6 (2014) 18735–18741.

[21] R. Sha, N. Vishnu, S. Badhulika, MoS_2 based ultra-low-cost, flexible, non-enzymatic and non-invasive electrochemical sensor for highly selective detection of Uric acid in human urine samples, Sensor. Actuat. B-Chem. 279 (2019) 53–60.

[22] J.C. Yao, Y.N. Quan, R.X. Gao, J. Li, L. Chen, Y. Liu, J.H. Lang, H. Shen, Y.Y. Wang, J.H. Yang, M. Gao, Improved charge transfer and hot spots by doping and modulating the semiconductor structure: a high sensitivity and renewability surface-enhanced raman spectroscopy substrate, Langmuir 35 (2019) 8921–8926.

[23] M. Gao, C. Yan, B.Z. Li, L.J. Zhou, J.C. Yao, Y.J. Zhang, H.L. Liu, L.H. Cao, Y.T. Cao, J.H. Yang, Y.X. Wang, Strong red emission and catalytic properties of ZnO by adding Eu_2O_3 shell, J. Alloys. Compd. 724 (2017) 537–542.

[24] S. Yang, J.C. Yao, Y.N. Quan, M.Y. Hu, R. Su, M. Gao, D.L. Han, J.H. Yang, Monitoring the charge-transfer process in a Nd-doped semiconductor based on photoluminescence and SERS technology, Light Sci. Appl. 9 (2020) 117.

[25] M.A. Dwiputra, F. Fadhila, C. Imawan, V. Fauzia, The enhanced performance of capacitive-type humidity sensors based on ZnO nanorods/WS_2 nanosheets heterostructure, Sensor. Actuat. B-Chem. 310 (2020), 127810.

[26] Y.N. Quan, J.C. Yao, S. Yang, L. Chen, J. Li, Y. Li, J.H. Lang, H. Shen, Y.X. Wang, Y. Y. Wang, J.H. Yang, M. Gao, ZnO nanoparticles on MoS_2 microflowers for ultrasensitive SERS detection of bisphenol A, Microchim. Acta 186 (2019) 593.

[27] X.Y. Xu, X.F. Dong, Z.J. Bao, R. Wang, J.G. Hua, H.B. Zeng, Three electron channels toward two types of active sites in MoS_2@Pt nanosheets for hydrogen evolution, J. Mater. Chem. A Mater. Energy Sustain. 5 (2017) 22654–22661.

[28] X.N. Zhao, Y.C. Lei, P.F. Fang, H.J. Li, Q. Han, W.G. Hu, C.Q. He, C_2H_5OH and NO_2 sensing properties of ZnO nanostructures: correlation between crystal size, defect level and sensing performance, Nano Energy 66 (2019), 104168.

[29] P.D. Fleischauer, J.R. Lince, A comparison of oxidation and oxygen substitution in MoS_2 solid film lubricants, Tribol. Int. 32 (1999) 627–636.

[30] C.Y. Li, Y.Q. Huang, K.Q. Lai, B.A. Rasco, Y.X. Fan, Analysis of trace methylene blue in fish muscles using ultra-sensitive surface-enhanced Raman spectroscopy, Food Control 65 (2016) 99–105.

[31] J.C. Yao, Y.N. Quan, M. Gao, R.X. Gao, L. Chen, Y. Liu, J.H. Lang, H. Shen, Y. J. Zhang, L.L. Yang, J.H. Yang, AgNPs decorated Mg-doped ZnO heterostructure with dramatic SERS activity for trace detection of food contaminants, J. Mater. Chem. C Mater. Opt. Electron. Devices 7 (2019) 8199–8208.

[32] Y. Zhan, Y.L. Liu, H.R. Zu, Y.X. Guo, S.S. Wu, H.Y. Yang, Z.M. Liu, B.F. Lei, J. L. Zhuang, X.J. Zhang, D. Huang, C.F. Hu, Phase-controlled synthesis of molybdenum oxide nanoparticles for surface enhanced Raman scattering and photothermal therapy, Nanoscale 10 (2018) 5997–6004.

[33] A. Moeinian, F.N. Gür, J. Gonzalez-Torres, L. Zhou, V.D. Murugesan, A. D. Dashtestani, H. Guo, T.L. Schmidt, S. Strehle, Highly localized SERS measurements using single silicon nanowires decorated with DNA origami-based SERS probe, Nano Lett. 19 (2019) 1061–1066.

[34] W.J. Li, Y.F. Ren, Y. Guo, ZrO_2/ZnO nanocomposite materials for chemiresistive butanol sensors, Sensor. Actuat. B-Chem. 308 (2020), 127658.

[35] Y. Zeng, N. Guo, Y.J. Song, Y. Zhao, H.Y. Li, X.J. Xu, J.D. Qiu, H.W. Yu, Fabrication of Z-scheme magnetic MoS_2/$CoFe_2O_4$ nanocomposites with highly efficient photocatalytic activity, J. Colloid. Interf. Sci. 514 (2018) 664–674.

[36] H.D. Aghdam, S.M. Bellah, R. Malekfar, Surface-enhanced Raman scattering studies of Cu/Cu_2O Core-shell NPs obtained by laser ablation, Spectrochim. Acta A. 233 (2019), 117379.

[37] M. Gao, J.C. Yao, C. Yan, X.F. Li, T.J. Hu, L. Chen, Y.X. Wang, Y.J. Zhang, H.L. Liu, Y. Liu, L.H. Cao, Y.T. Cao, J.H. Yang, Novel composite nanomaterials with superior thermal and pressure stability for potential LED applications, J. Alloys. Compd. 734 (2018) 282–289.

[38] D.C. Look, J.W. Hemsky, J.R. Sizelove, Residual native shallow donor in ZnO, Phys. Rev. Lett. 82 (1999) 2552–2555.

[39] P. Zuo, L. Jiang, X. Li, B. Li, Y.D. Xu, X.S. Shi, P. Ran, T.B. Ma, D.W. Li, L.T. Qu, Y. F. Lu, C.P. Grigoropoulos, Shape-Controllable Gold Nanoparticle–MoS_2 Hybrids Prepared by Tuning Edge-Active Sites and Surface Structures of MoS2 via Temporally Shaped Femtosecond Pulses, ACS Appl. Mater. Inter. 9 (2017) 7447–7455.

[40] X. Ling, W. Fang, Y.H. Lee, P.T. Araujo, X. Zhang, J. FRodriguez-Nieva, Y. Lin, J. Zhang, J. Kong, M.S. Dresselhaus, Raman enhancement effect on two-dimensional layered materials: graphene, h-BN and MoS_2, Nano Lett. 14 (2014) 3033–3040.

[41] X.J. Tan, L.Z. Wang, C. Cheng, X.F. Yan, B. Shena, J.L. Zhang, Plasmonic MoO_{3-x}@MoO_3 nanosheets for highly sensitive SERS detection through nanoshell-isolated electromagnetic enhancement, Chem. Commun. (Camb.) 52 (2016) 2893–2896.

[42] N. Singh, J. Prakash, M. Misra, A. Sharma, R.K. Gupta, Dual functional Ta-Doped electrospun TiO2 nanofibers with enhanced photocatalysis and SERS detection for organic compounds, ACS Appl. Mater. Inter. 9 (2017) 28495–28507.

[43] Y.F. Shan, Z.H. Zheng, J.J. Liu, Y. Yang, Z.Y. Li, Z.R. Huang, D.L. Jiang, Niobium pentoxide: a promising surface-enhanced Raman scattering active semiconductor substrate, npj, Comput. Mater. 3 (2017) 11.

[44] H. Wu, H. Wang, G.H. Li, Metal oxide semiconductor SERS-active substrates by defect engineering, Analyst 142 (2017) 326–335.

[45] H.S. Lai, G.R. Ma, W.J. Shang, D.J. Chen, Y.Y. Yun, X. Peng, F.G. Xu, Multifunctional magnetic sphere-MoS_2@Au hybrid for surface-enhanced Raman scattering detection and visible light photo-Fenton degradation of aromatic dyes, Chemosphere 223 (2019) 465–473.

[46] L.L. Xu, H. Zhang, Y. Tian, A.X. Jiao, F. Chen, M. Chen, Photochemical synthesis of ZnO@Au nanorods as an advanced reusable SERS substrate for ultrasensitive detection of light-resistant organic pollutant in wastewater, Talanta 194 (2019) 680–688.

[47] J.L. Chen, K. Sun, Y. Zhang, D. Wu, Z. Jin, F.Z. Xie, X.L. Zhao, X.F. Wang, Plasmonic MoO_2 nanospheres assembled on graphene oxide for highly sensitive SERS detection of organic pollutants, Anal. Bioanal. Chem. 411 (2019) 2781–2791.

Yingnan Quan received her BSc degree in physics at Jilin Normal University in 2014. At present, she is studying optics at Jilin Normal University. She is now a second-year postgraduate student under the supervision of A.P. Ming Gao. Her current interests are focused on the development of modified semiconductor materials in the field of surface-enhanced Raman spectroscopy (SERS). In particular, she had a lot of work on practical applications of SERS.

Ming Gao received her doctoral degrees in condensed matter physics at University of Chinese Academy of Sciences. After she was a postdoc in the School of Engineering and Applied Sciences (SEAS) at Harvard University. She has been conducting research in optical in the Physics Department of Jilin Normal University as an associate professor. Her main research focuses on surface enhanced spectroscopic techniques, e.g. the generation of powerful SERS substrates and their application to food security and environmental analytical questions; nanomaterials and applications in solid state lighting.